Suplementary material of the article titled: Comparison of Spectral Multi-material Phase Retrieval Algorithms based on Edge Illumination Single Mask X-ray Phase Contrast Imaging

1. Experimental comparison

To evaluate the suitability of both approaches while accounting different experimental non-idealities, a micro-focus Hamamatsu L6622-01 is used, with a tungsten target and a minimal focal spot of 10 μm. The source is operated at a current of 71 μA and a voltage of 28 kVp, using a filter of Aluminum 1 mm thick to avoid the contribution of photons with energies lower than 10 keV.

The X-ray detector employed is a Timepix3, paired to a 1 mm thick CdTe sensor, which consists of a 256x256 matrix of square pixels with a pixel pith of 55 μm. Operated with a bias voltage of -300 V and an energy threshold of 4.96 keV, the ToT (time-over-threshold)-ToA (time of arrival) mode is used, enabling the acquisition of sample images in different energy bins within a single X-ray exposure. In this configuration, four energy-bin images are acquired, each corresponding to a distinct energy range: 13–16 keV, 17–20 keV, 21–24 keV, and 25–28 keV. The average energy for each energy bin image is calculated based on the detected photon energy distribution within the corresponding range. To correct the charge sharing effect, a clustering algorithm is employed. The detector is positioned 75.45 cm away from the X-ray source.

The sample consisted of a hollow PMMA tube, with internal (external) diameter of 3 mm (3.85 mm). The sample is positioned downstream of the EI mask, at a distance of 58.25 cm from the X-ray source. The EI mask is composed of a periodic structure consisting of micrometer gold rods, galvanized on a graphite substrate 500 μm thick and regularly spaced with a period of 79 μm. To achieve the EI condition, the mask is positioned at 53.35 cm from the X-ray source. The number of steps to obtain the complete image is 8.

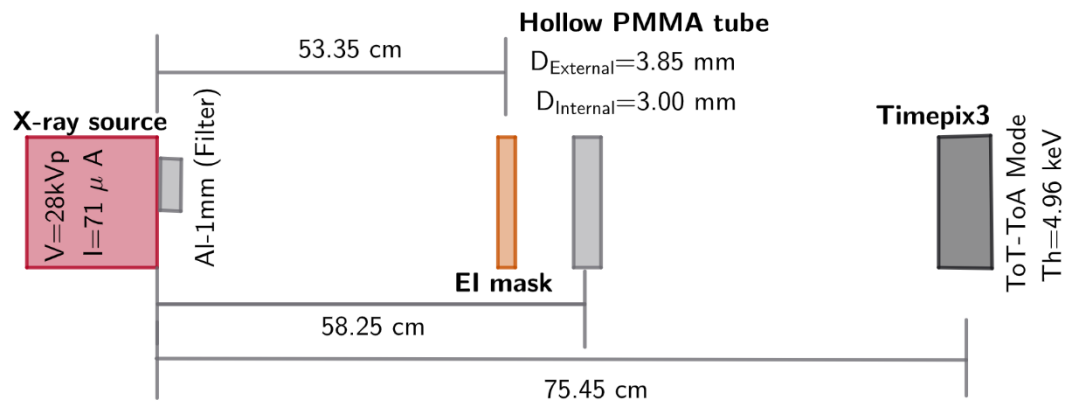Figure S1 schematically illustrates the experimental setup.

Figure S1. Experimental setup, where the X-ray source, the sample, the mask, and the detector are illustrated.

The application of equations 9, 11, 12, and 15 allows for the retrieval of the projected thickness using the different approaches. The same process presented in the manuscript is followed with the experimental data. The prior knowledge of the total projected thickness is derived from the dimension of the external diameter; therefore, a solid cylinder with a

diameter of 3.85 mm is built in Python and used as Z_o in equations 6 and 13. As a single material is embedded (Air) within the encasing material (PMMA), the information of the $\vartheta = 4$ input images is used in equations 9, 11, 12, and 15 to retrieve the projected thickness of air, with $\Omega - 1 = 1$ and $\Delta\beta_2 = \beta_{Air} - \beta_{PMMA}$ ($\Delta\delta_2 = \delta_{Air} - \delta_{PMMA}$). To construct the Υ matrix and the ζ function, $\bar{S}_B$ and σ_B are calculated in red circular region of interest (ROI), while $\bar{S}_R$ is calculated in the blue ROI, as illustrated in Figure S2.
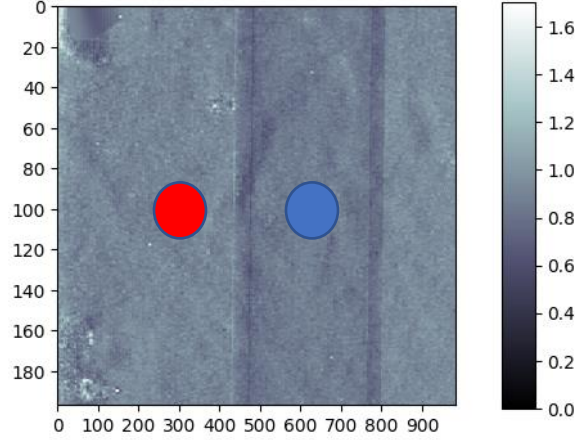

Figure S2. Visualization of the regions selected in the CI_- image at the energy-bin 13–16 keV for evaluating the Y matrix and the ζ function.

Figure S3 presents the projected thickness retrieved by the Beltran approach at the energy-bin 17–20 keV (left), the spectral multi-material decomposition approach (center) and the energy-weighted Beltran approach (right).
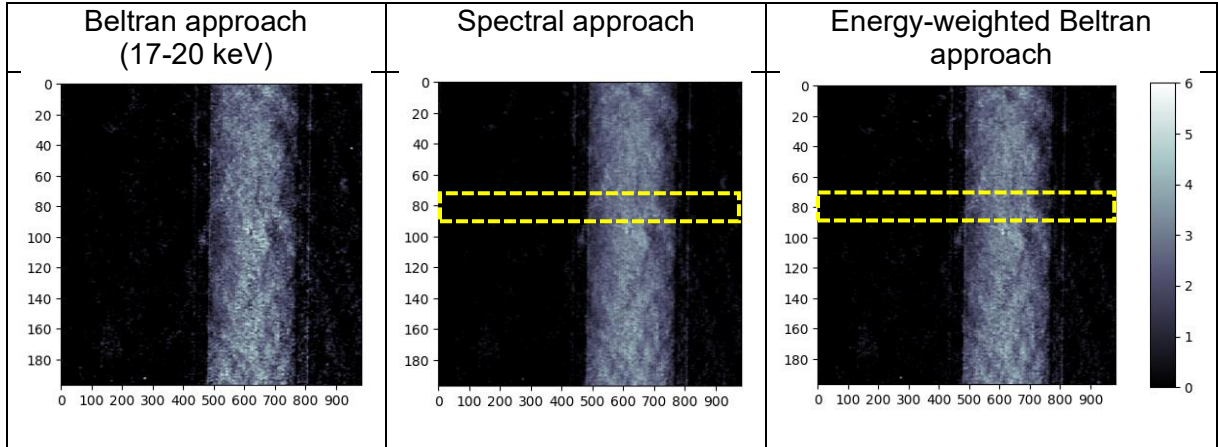

Figure S3. Retrieved projected thickness map of air obtained using the Beltran approach at the energy-bin 17-20 keV (left), the spectral multi-material decomposition approach (center) and the energy-weighted Beltran approach (right) with the $CI_\pm$ images.

To evaluate the trend of the projected thickness retrieved for each approach, the projected thickness profiles are depicted, defined as the projections of the thickness maps within the selected yellow regions shown in Figure S3.
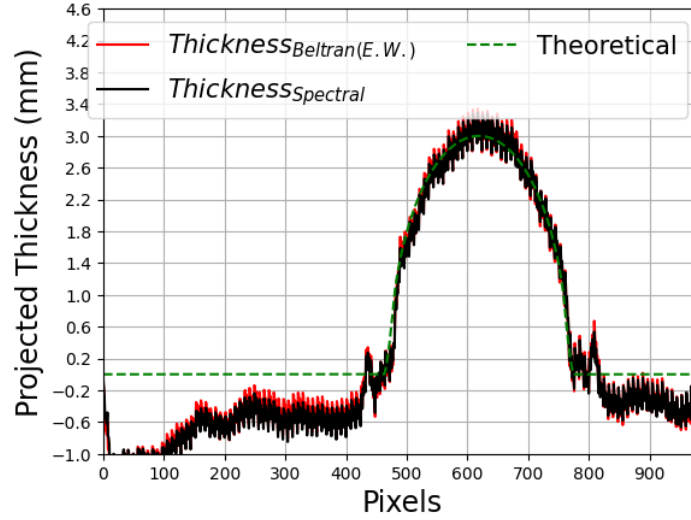
Figure S4. Comparison of the retrieved and theoretical projected thickness profiles.

In this part, it is verified that both approaches retrieve the projected air thickness, as they follow the expected behavior.

Analyzing the CNR values in the projected thickness maps, calculated using the same regions for the ζ function, Figure S5 demonstrates that the CNR of the thickness maps are higher than those in the CI_- images, and the CNR obtained by the spectral multi-material decomposition approach is higher than that obtained with the Beltran and energy-weighted Beltran approaches. This is an experimental demonstration that the spectral approach outperforms the Beltran approach in visualizing features with higher CNR when the same number of $CI_\pm$ images and equivalent absorbed dose conditions are used to estimate the projected thickness of a single material within the sample.
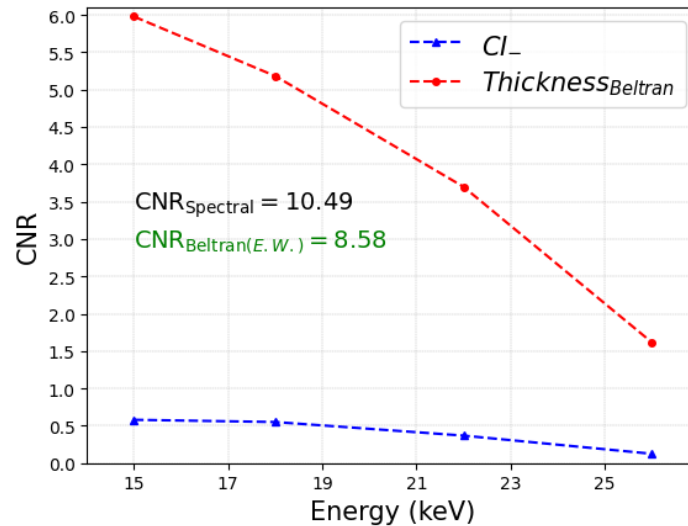

Figure S5. CNR of the inner cylinder in the $CI_\pm$ images (blue curve) and in the projected thickness maps obtained using the Beltran approach (red curve) at each energy-bin. CNR values obtained by the spectral multi-material decomposition and the energy-weighted Beltran approaches are also illustrated.